The Planetary Science Journal, 3:168 (9pp), 2022 July https://doi.org/10.3847/PSJ/ac7790
© 2022. The Author(s). Published by the American Astronomical Society.
OPEN ACCESS

Identifying Shadowing Signatures of C Ring Ringlets and Plateaus in Cassini Data from Saturn's Ionosphere

Joshua Dreyer[1,2], Erik Vigren[1], Fredrik L. Johansson[1], Oleg Shebanits[1], Michiko Morooka[1], Jan-Erik Wahlund[1], Rebecca S. Perryman[3], and Jack Hunter Waite[3]
[1] Swedish Institute of Space Physics (IRF), Uppsala, Sweden; joshua.dreyer@irfu.se
[2] Department of Physics and Astronomy, Uppsala University, Uppsala, Sweden
[3] Space Science and Engineering Division, Southwest Research Institute, San Antonio, USA
Received 2021 August 11; revised 2022 May 19; accepted 2022 June 8; published 2022 July 20

Abstract

For orbits 288 and 292 of Cassini's Grand Finale, clear dips (sharp and narrow decreases) are visible in the H_2^+ densities measured by the Ion and Neutral Mass Spectrometer (INMS). In 2017, the southern hemisphere of Saturn was shadowed by its rings and the substructures within. Tracing a path of the solar photons through the ring plane to Cassini's position, we can identify regions in the ionosphere that were shadowed by the individual ringlets and plateaus (with increased optical depths) of Saturn's C ring. The calculated shadowed altitudes along Cassini's trajectory line up well with the dips in the H_2^+ data when adjusting the latter based on a detected evolving shift in the INMS timestamps since 2013, illustrating the potential for verification of instrument timings. We can further estimate the mean optical depths of the ringlets/plateaus by comparing the dips to inbound H_2^+ densities. Our results agree well with values derived from stellar occultation measurements. No clear dips are visible for orbits 283 and 287, whose periapsides were at higher altitudes. This can be attributed to the much longer chemical lifetime of H_2^+ at these higher altitudes, which in turn can be further used to estimate a lower limit for the flow speed along Cassini's trajectory. The resulting estimate of $\sim$0.3 km s^{-1} at an altitude of $\sim$3400 km is in line with prior suggestions. Finally, the ringlet and plateau shadows are not associated with obvious dips in the electron density, which is expected due to their comparatively long chemical (recombination) lifetime.

Unified Astronomy Thesaurus concepts: Saturn (1426); Space plasmas (1544); Planetary ionospheres (2185); Planetary rings (1254)

1. Introduction

The Saturnian system is a prime example of complex interactions between a planet, its moons, and the resulting structured rings, and not all features are explained as of yet (see, e.g., Colwell et al. 2009; Cuzzi et al. 2018). Gaps in Saturn's rings were first observed by the Italian scientist Giovanni Domenico Cassini in 1675. Recently, and rather fittingly, the Cassini–Huygens mission has provided unprecedented insight into the finer details of Saturn and its moons and rings and expanded our understanding of their interactions (e.g., Waite et al. 2018; Hsu et al. 2018; Hunt et al. 2018). With its Grand Finale in 2017, Cassini offered the first ever in situ measurements of Saturn's ionosphere. During the last six orbits Cassini dove to altitudes below 2000 km (with respect to the 1 bar level, which is 60,268 km from Saturn's center at the equator), crossing an ionospheric peak during the final plunge (Hadid et al. 2019). Electron density profiles in the upper ionosphere were observed to be highly variable (Wahlund et al. 2018). The ionosphere can generally be categorized into three layers/regions (Hadid et al. 2019; Persoon et al. 2019). The uppermost is a transport-dominated region above 4500 km, with low densities and long mean free paths. Below this, down to altitudes of $\sim$2200–2500 km, exists a diffusive equilibrium region, where an influx of ring particles near the equatorial plane (and at higher latitudes, see O'Donoghue et al. 2017) significantly affects the ionospheric chemistry. Finally, the ionosphere below $\sim$2200–2500 km is dominated by chemical processes and can thus be treated as in photochemical equilibrium. Infalling grains from the D ring (Mitchell et al. 2018) have been connected to a significant level of electron depletion and heating (Morooka et al. 2019). Additionally, the overall chemistry shows several surprising dominant ion species heavier than H_3^+ that are likely a result of the infalling material (Moore et al. 2018), which spans a broad mass spectrum range (Waite et al. 2018).

Identifying the ring effects within data from Cassini's deep dives into the ionosphere does not always require chemical analysis. A clear ring shadowing signature can be seen in the electron densities as measured by the Langmuir probe (part of the Radio and Plasma Waves Science instrument suite (RPWS); see Gurnett et al. 2004) in the southern hemisphere, where the shadow of the dense B ring mapped to the ionosphere at the time (Hadid et al. 2018). The resulting decrease in extreme ultraviolet (EUV) flux due to the opacity of the B ring manifests as lower electron and ion densities within these shadowed regions. A similar shadowing effect on the electron number density is observed for the A ring, but not for the more tenuous C and D rings (Hadid et al. 2018).

The present study investigates potential signatures of ringlets and plateaus within the C ring in data from the Ion and Neutral Mass Spectrometer (INMS; see Waite et al. 2004), specifically in the observed H_2^+ densities. As the chemical lifetime of H_2^+ at the analyzed altitudes (at least for orbits 288 and 292, which reached altitudes <2500 km) is $\lesssim$1 s, and the production of H_2^+ is directly proportional to the amount of incoming solar EUV flux, the H_2^+ density can be used as a good proxy for the EUV

Original content from this work may be used under the terms of the Creative Commons Attribution 4.0 licence. Any further distribution of this work must maintain attribution to the author(s) and the title of the work, journal citation and DOI.

flux and will decrease rapidly in shadowed regions. At higher altitudes, this lifetime increases and thus transport processes disturb the balance between production through photoionization and chemical loss. Dips (used further to describe sharp and narrow decreases) in the H_2^+ density for the outbound part of orbit 292 were described in Dreyer et al. (2021), who suggested ringlet shadowing signatures as a potential explanation, which we will further study here. We adopt the terminology of Colwell et al. (2009): ringlets (R) as narrow rings with increased optical depth within gaps where the background optical depth drops to practically zero, embedded ringlets (ER) as regions with prominent increases in optical depth compared to the background optical depth profile (but not offset from it by a gap), and plateaus (P) denoting embedded ringlets with optical depths of $\tau \sim 0.4$ rising sharply from the background and peak optical depths at the edges (see Figure 1 in Jerousek et al. 2020).

Cassini data and the analysis methods are briefly presented in the following Section 2, and the respective results are further discussed in Section 3. Finally, our conclusions are summarized in Section 4. The Appendices contain information on methodology, additional data, and a description of a detected INMS timestamp shift.

2. Data and Methods

The INMS-measured ion and neutral number densities during Cassini's Grand Finale (Waite et al. 2018), continuously cycling between the two modes for the orbits described here. Due to the constraints of the instrumentation and the high spacecraft velocity ($\sim$34 km s^{-1}), only the number densities of ions up to 8 Da are available. Of these, H_2^+ is the ion of particular interest for this study, as it is essentially a proxy for the solar EUV flux due to its short chemical lifetime (reacting with H_2 to produce H_3^+) and being produced predominantly through photoionization of H_2:

$$H_2 + h\nu \rightarrow H_2^+ + e^- \quad (1)$$

$$H_2^+ + H_2 \rightarrow H_3^+ + H. \quad (2)$$

Number densities of H_2^+ are available for orbits 283, 287, 288, and 292, which are analyzed in the present study.

Tracing the path of the solar photons through the rings into Saturn's ionosphere allows the determination of the shadowed altitudes along Cassini's trajectory for any given part of the rings. The hour angle, planetocentric latitude, and distance from Saturn's center in 1 s steps for each respective Cassini orbit are obtained from the Cassini ephemeris tool (NASA Planetary Data System (PDS) ; see acknowledgments). The 1 bar level and Cassini's altitude above it are based on the gravity-corrected model by Militzer et al. (2019). Figure 1 shows the obtained latitudes and hour angles at the corresponding Cassini altitudes for the outbound parts of the four analyzed orbits, which is the portion of the flybys in the southern hemisphere, where the ring shadows fell.

The radial distance where the light ray from the Sun to Cassini crosses the ring plane at any given Cassini position can be calculated as

$$R_{\rm cross} = R_{\rm Cass} \times \sqrt{\left(\cos\theta \times \cos h_\odot + \frac{\sin|\theta|}{\tan\phi_\odot}\right)^2 + (\cos\theta \times \sin h_\odot)^2}\ , \quad (3)$$

with Cassini's distance from Saturn's center $R_{\rm Cass}$, planetocentric subspacecraft latitude θ, solar hour angle $h_\odot$ (subsolar minus subspacecraft rotating longitude), and subsolar latitude $\phi_\odot$. These variables are visualized in Figure 2, which also serves as a visual aid to follow the derivation of Equation (3) presented in Appendix A.

Cassini's shadow crossing altitudes for the outbound parts of the four orbits are plotted as a function of the solar photon's ring crossing distance $R_{\rm cross}$ in Figure 3. Fitting a quartic polynomial for each orbit (see Appendix B), we can now insert any known ringlet/plateau distance as $R_{\rm cross}$ and obtain the projected shadowed altitude along Cassini's trajectory $A_{\rm Cass}$ (Equation (B1)) for each orbit. Inserting the inner and outer ringlet/plateau edge distances as given in Table 1 results in an altitudinal shadow entry and exit point along Cassini's trajectory for each ringlet/plateau.

Initial comparisons between the calculated shadowed altitudes and observed H_2^+ dips indicated an offset between the two, which appeared to stay almost constant over the altitude range considered. This indicates a systematic error, either in the calculated altitudes or the observations. Indeed, further investigation revealed that the INMS ion timestamps are shifted by a few seconds, with the offset varying over the mission and steadily increasing since 2013. This is further discussed in Appendix C, with an illustration in Figure 6. For orbits 288 and 292, the offsets are -4.87 and -5.03 s, respectively. In the subsequent steps, we will proceed by shifting the INMS timestamps as outlined in Appendix C.

3. Results and Discussion

The results for orbits 288 and 292 are presented in Figure 4, which shows clear shadowing signatures in the H_2^+ number densities for both orbits. All major dips align well with the calculated ringlet/plateau shadows (once adjusted for the timestamp offset described above). The INMS H_2^+ data points that fall within a shadowed altitude region along Cassini's trajectory are colored red. Generally, the overall variance in H_2^+ densities is likely a combination of statistical spread and measurement error, as the measured densities are very low and the spacecraft moves through the ionosphere at a high speed. Nonetheless, the shadowing signatures of most ring features are still visible as discernible decreases.

Some ringlets/plateaus do not show any associated drop in density; for the Titan ringlet and P4 plateau, this can be explained by their small width of 40 and 45 km, respectively, which results in an altitudinal shadow extent (vertical distance along Cassini's trajectory between the intersection of calculated solar ray crossings from the inner and outer edges of any given ring feature) of only $\sim$1 km (see Table 1) along Cassini's trajectory. The detection of potential shadow signatures is dependent on the temporal, and therefore spatial, resolution of the INMS data set. Not only would there have to be an INMS ion measurement at precisely the right position (INMS cycled

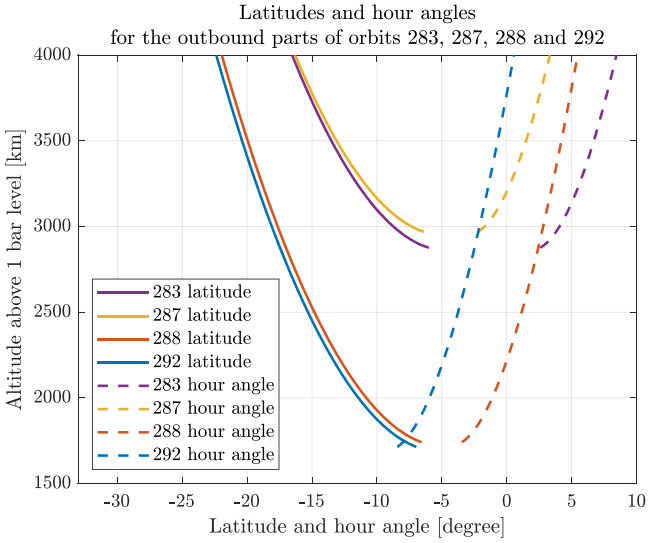

Figure 1. Cassini's altitudes above the 1 bar level for a range of planetocentric subspacecraft latitudes and solar hour angles (subsolar minus subspacecraft rotating longitude) for orbits 283, 287, 288, and 292. Only the outbound parts after closest approach for each orbit are shown because the ring shadows fell in the southern hemisphere.

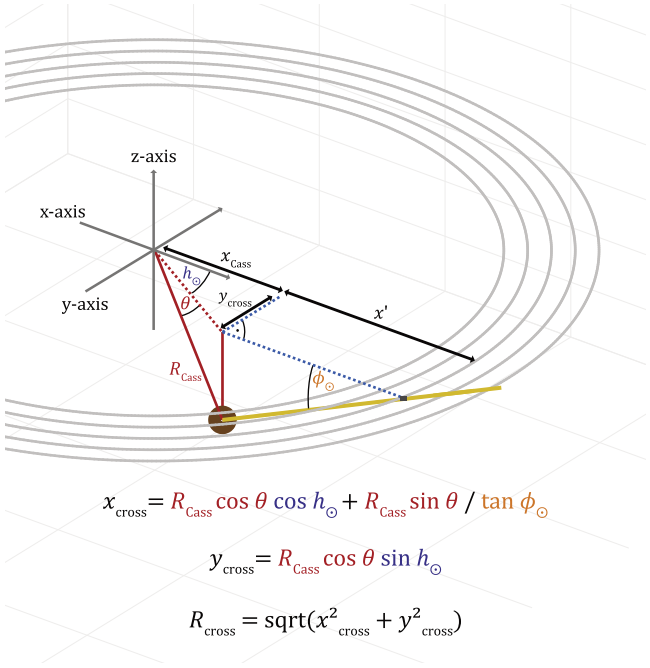

Figure 2. The right-hand planetocentric coordinate system is such that the z-axis runs through the polar axis of Saturn while the xy-plane contains the ring plane. Moreover, the x- and y-axes are so organized that along any given ray path the y-axis value is constant, which is to say that the Sun is in the xz-plane. In fact, for a solar elevation angle of zero, the x-axis would coincide with the extended line through Saturn and the Sun. Justified by the large distance to the Sun, we treat the rays as collimated for geometry purposes (penumbra can then be considered as a perturbation). This figure is meant as a graphical derivation of Equation (3); see further Appendix A. Note that the three dashed lines are all characterized by $z = 0$ and that the sought $R_{cross} = x_{Cass} + x'$ is obtained by finding the distance from the center to the intersection point of a relevant ray path (yellow solid line) with the blue dashed line (marked with a dark gray square). Note finally that our geometric derivation is one wherein all angles are treated as positives. However, as seen in Equation (3) it is sufficient to invoke an absolute sign around an angle only at one instance.

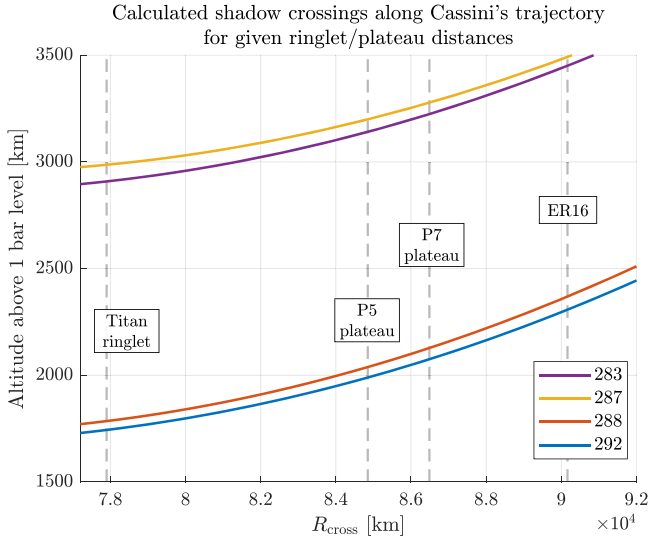

Figure 3. Calculated shadowed altitudes along Cassini's trajectory (A_{Cass}) as a function of the radial distance of rays crossing the ring plane (R_{cross}) for orbits 283, 287, 288, and 292. The intersection of known ringlet/plateau positions (examples as vertical dashed lines) with the R_{cross} function Equation (3) for each orbit can be used to find the shadowed altitudes, although in practice this is done with a polynomial fit function as described in Appendix B.

between ion and neutral mode, creating 4.6 s gaps separating the individual ion data cycles), but the shadows of these two features might be too narrow, with the rotation of the planet moving the measured plasma volume out of the shadow at timescales smaller than the lifetime of the H_2^+ ions (which are $\lesssim$0.5 s near periapsis; see further discussion below). The shadows of most other ringlets and plateaus are clearly visible in the INMS H_2^+ data for orbit 292 in Figure 4, despite only being between 5 and 16 km in altitudinal extent along Cassini's trajectory. For instance, while casting shadows with altitudinal extents of only ~5 km along Cassini's trajectory, clear signatures of both the Maxwell and ER16 ringlets are seen in the H_2^+ data from orbit 292. Notable exceptions are the P8 and P9 plateaus, for which neither orbit 288 nor 292 show any shadowing signature (in Figure 4). On closer inspection, it is evident that INMS was measuring neutrals and not ions when Cassini was traversing the shadowed altitudes of these two plateaus, explaining the lack of visible ion signatures.

The dips in the H_2^+ number densities can be used to roughly estimate the optical depths of the ringlets/plateaus, to be compared with measurements from stellar occultations (e.g., Jerousek et al. 2020). To this end, we need H_2^+ number densities outside of any ring shadowing, which were measured during the inbound part of each orbit. Since H_2^+ is produced through photoionization of H_2 and lost quickly by reacting with H_2 to produce $H_3^+ + H$, we can assume H_2^+ densities outside of the ring shadows to be comparable to the inbound orbit part if the H_2 profiles do not vary significantly. They indeed do not, and thus we adapt the H_2^+ fit derived by Dreyer et al. (2021) for the inbound part of orbit 292 to estimate the arriving solar EUV flux when it is not passing through Saturn's rings. For this purpose, we refit the H_2^+ number densities (per cubic centimeter) as a function of altitude (in kilometers), as the original fit was derived as a function of H_2 densities. The respective fit parameters are listed in Table 2; see Appendix B. The lower number of H_2^+ data points for orbit 288 makes it difficult to use for the same purpose, and we thus refrain from attempting this. As the

Table 1
Selected C Ring Ringlets and Plateaus and Their Calculated Shadowed Altitudes along Cassini's Orbit (Rounded to the Nearest Integer) for Orbit 292, As Shown in Figure 3

Name	Inner Edge (km)	Outer Edge (km)	Width (km)	Shadow Lower Altitude (km)	Shadow Upper Altitude (km)	Shadow Altitudinal Extent (km)	$\bar{\tau}_n \pm \sigma$ (J20)	$\bar{\tau}_n \pm \sigma$ from H_2^+ Data
R_{Titan}	77880	77920	40	1743	1744	1	0.4–5.9 [1]	⋯
P4	79220	79265	45	1776	1777	1	0.44 ± 0.01	⋯
P5	84750	84950	200	1984	1994	10	0.43 ± 0.01	0.44 ± 0.14
P6	85660	85755	95	2031	2036	5	0.33 ± 0.01	0.36 ± 0.06
P7	86375	86605	230	2069	2082	13	0.40 ± 0.01	0.43 ± 0.09
$R_{Maxwell}$	87500	87590	90	2134	2139	5	0.97 [2]	0.49 ± 0.18
P8	88350	88595	245	2186	2202	16	0.25 ± 0.02	0.20
P9	89190	89295	105	2241	2248	7	0.27 ± 0.01	⋯
P10	89790	89940	150	2281	2292	11	0.32 ± 0.01	0.27 ± 0.13
ER16	90130	90200	70	2305	2310	5	large $\Delta\bar{\tau}_n$	0.44 ± 0.19
P11	90405	90610	205	2325	2341	16	0.37 ± 0.02	0.39 ± 0.07

Note. Inner and outer edges and widths are adapted from Table 13.4 in Colwell et al. (2009). The estimated mean normalized optical depths $\bar{\tau}_n$ (see Equation (5)) are compared with optical depths derived from stellar occultation data (Jerousek et al. 2020, marked as J20). The mean optical depths for the Titan and Maxwell ringlets are given by [1] Jerousek et al. (2011) and [2] French et al. (2016), respectively. The inbound H_2^+ density (red line in Figure 4) is here assumed as fixed and not included in the specified margins of $\bar{\tau}_n$. These values are purely determined by taking the standard deviation of the data points in each shadowed bin, as the error for the inbound data is hard to quantify and based on multiple assumptions. Nonetheless, the results indicate that the estimation of $\bar{\tau}_n$ with this method produces very reasonable results. Note that there is only one H_2^+ data point in the calculated shadowed altitude range of the P8 plateau, and none for the P9 plateau.

H_2^+ density scales linearly with the solar EUV flux, the derived inbound number densities can then be compared with the measured outbound number densities for each ringlet/plateau shadow altitude interval to estimate the mean optical depths of the respective ringlet/plateau, as follows:

$$\bar{\tau} = \mathrm{mean}(-\ln([H^+_{2,\mathrm{meas}}]/[H^+_{2,\mathrm{fit}}])). \quad (4)$$

This is an adaptation of the general definition of optical depth $\tau = -\ln(T)$, where the transparency T is the ratio between the occulted and unocculted signal (e.g., Nicholson et al. 2020). Furthermore, the normal optical depth τ_n is a representation of what the optical depth would be if the rings were viewed face-on, accounting for any slanted ray paths:

$$\bar{\tau}_n = \bar{\tau} \times \sin(\phi_\odot). \quad (5)$$

The results of this estimation are listed for the analyzed ringlets/plateaus in Table 1. Considering this simple method, the derived $\bar{\tau}_n$ agree remarkably well with those derived from stellar occultation measurements by Jerousek et al. (2020). The mean optical depths are calculated by taking the mean of the calculated optical depth according to Equation (5) for each H_2^+ data point in each shadowing bin. The given standard deviations are calculated in the same manner and do not include the systematic error from the use of a fitted inbound H_2^+ profile (red line in Figure 4), which is based on multiple assumptions and hard to quantify. This method can be used to calculate the normal optical depth profile across the C ring, as shown in Figure 5. Comparing with Figure 1 in Jerousek et al. (2020) shows that our derived estimates for the background optical depth profile generally exceed the stellar occultation measurements by up to a factor of ∼2, but it should be noted that due to the variable H_2^+ densities it is impossible to derive a precise background profile. At higher altitudes, photochemical equilibrium does not apply and thus this method would not work for these regions, for example, to estimate the B ring optical depth profile.

We do not see responses of the ringlet shadows on the electron number densities, shown as gray dots in Figures 4 and 8. While the gaps in the high-frequency electron measurements could in theory hide shadowing signatures, an obvious response is not seen even where data points are present in calculated shadowing regions and likely is not to be expected due the comparatively long chemical lifetime of free electrons. As an example, focusing on orbit 292 and its passage through the shadow of the P7 plateau at altitudes of 2070–2080 km (see Figure 3), where the H_2 number density is $n_n \approx 10^9$ cm^{-3} and the total ion number density is $n_i \approx 4 \times 10^3$ cm^{-3} (see Figure 1 of Dreyer et al. 2021), the chemical lifetimes for H_2^+ and free electrons are ∼0.5 and $\gtrsim$1000 s, respectively. These estimates follow from $1/(k_1 n_n)$ and $1/(\alpha n_i)$, where $k_1 = 2 \times 10^{-9}$ cm^3 s^{-1} (Theard & Huntress 1974) is the rate constant for the reaction $H_2^+ + H_2 \rightarrow H_3^+ + H$, and α is the effective ion–electron recombination rate coefficient, for which a utilized value of 2×10^{-7} cm^3 s^{-1} is to be viewed as a high estimate in light of the recent analysis by Dreyer et al. (2021).

For orbits 283 and 287, no clear shadowing signatures are visible in the H_2^+ data (see Figure 8 in Appendix D). This is not surprising because of Cassini's higher altitude during these passes. To illustrate, Cassini crossed the shadow of the P8 plateau above 3330 km for these orbits (see Figure 3), at which the H_2 number density was less than 10^6 cm^{-3}. This gives a chemical lifetime of $\gtrsim$500 s for H_2^+, which seems to be long enough for transport processes to remove any clear shadowing signatures. Assuming that transport is solely responsible for the lack of shadowing signatures for these orbits, we can make a rough estimate for a lower limit of the ion flow speed. Cassini took ∼4 s to traverse the shadow of the P8 plateau (which has the largest extent and is thus suitable for estimation of a lower limit) during orbit 287. At a speed of 34 km s^{-1}, this means it covered a distance of ∼136 km. If we assume ion transport along the path of Cassini (mostly horizontal from north to south), the lack of ionospheric shadowing signatures then suggests an ion flow speed exceeding $\gtrsim$0.3 km s^{-1}, which corresponds to the ratio of 136 km divided by the chemical lifetime of H_2^+ ($\gtrsim$500 s at this altitude). For comparison,

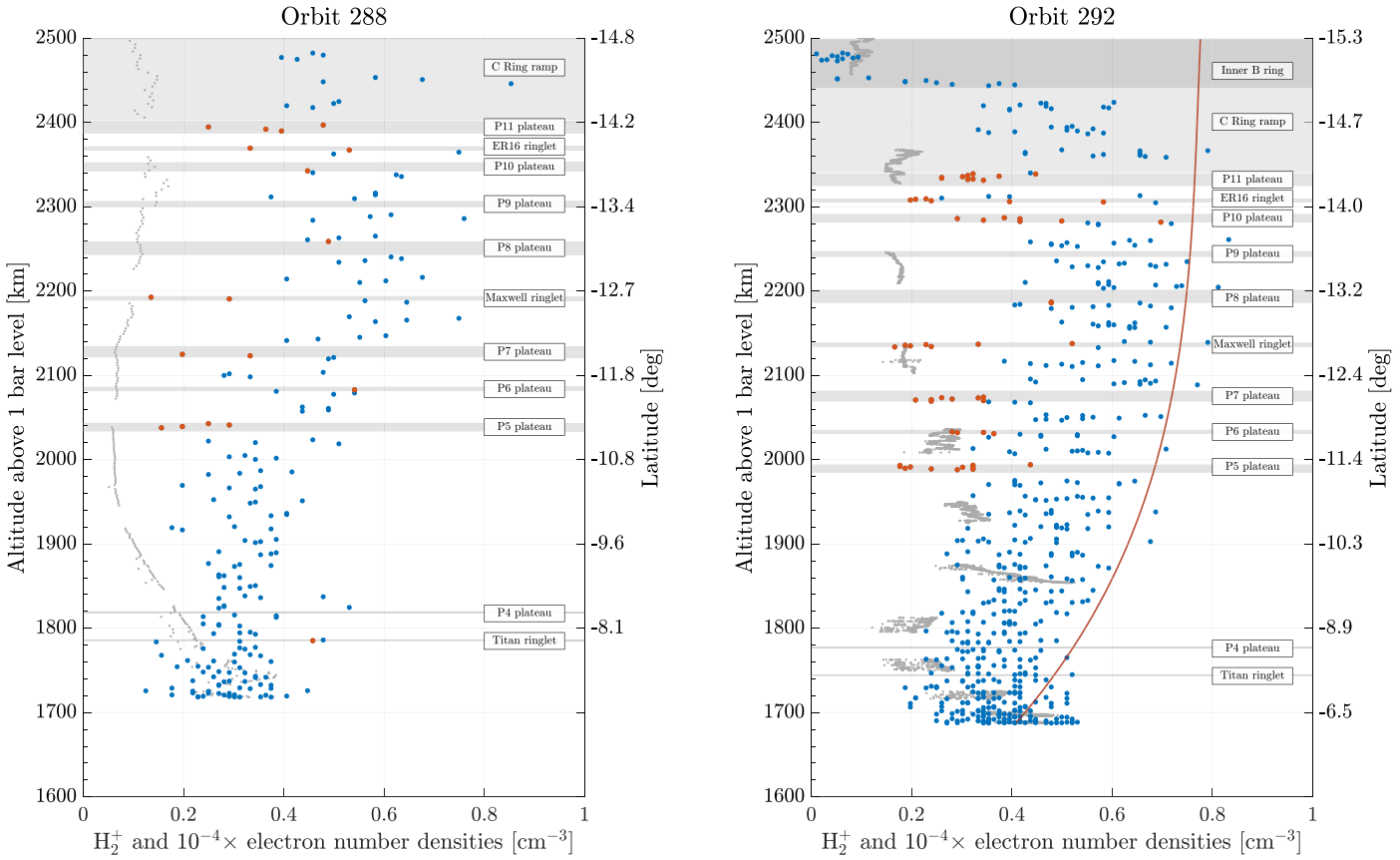

Figure 4. INMS-measured H_2^+ number densities for orbits 288 and 292 outbound between closest approach and 2500 km, using a time shift for the ion data as described in Appendix C. Electron data from the Langmuir probe are shown as gray dots with a scaling factor of 10^{-4}. The corresponding latitudes (see Figure 1) are given on the right-hand *y*-axes. Calculated shadows (in altitudinal extent along Cassini's trajectory) of major ringlets and plateaus in the C ring are shown as shaded areas, with the C ring ramp followed by the inner B ring visible at the upper altitudes. Data points within shadowed regions are colored red. The H_2^+ density fit for orbit 292 inbound data representing an H_2^+ profile unaffected by ring shadows, adapted from Dreyer et al. (2021), is shown as the solid red line.

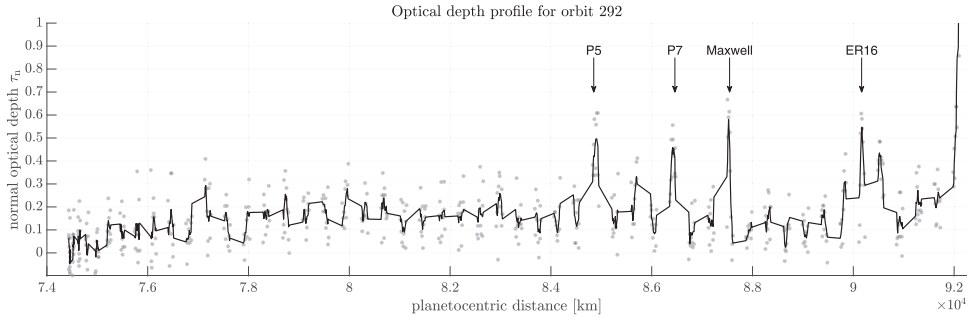

Figure 5. Calculated normal optical depth profile for the C ring, using H_2^+ data from orbit 292. Each measured data point is divided by the respective fitted unocculted density at the same altitude to derive the transparency *T*, which can then be inserted into Equations (4) and (5) (without taking a mean) to produce the individual gray points. A moving mean over five points is shown as the black line. The choice of window width for this moving mean will naturally affect the smoothness of the estimated optical depth profile.

Cravens et al. (2019) estimate a value for the magnetic field-aligned, meridional-directed ion flow speed of $\sim$1 km s^{-1} for the reached altitudes (and corresponding densities) during orbit 287. For orbit 292, where clear ionospheric shadowing signatures are visible in the H_2^+ data, one can by similar reasoning instead target an upper limit of the ion flow speed. However, due to the short chemical timescale of H_2^+ (a few seconds) at the relevant altitudes (and corresponding H_2 densities), these upper limits are far higher than likely values (e.g., an ion flow speed in excess of 17 km s^{-1} would be required for transport to dilute ionospheric shadowing signatures of ER16 during orbit 292).

4. Conclusions

In the present study, we describe the identification of C ring ringlet/plateau shadowing signatures in Cassini INMS data from Saturn's ionosphere. The observed dips in H_2^+ density for orbits 288 and 292 line up very well with the shadowed altitudes along Cassini's trajectory calculated from Equation (3). What initially seemed to be a systematic offset is shown to be the result of an INMS timestamp shift as described in Appendix C. Thus we have also shown that these ionospheric small-scale shadowing signatures can be used to verify instrument timestamps with high precision. After

correcting for this offset, the calculated shadowed altitudes along Cassini's trajectory precisely match the dips in H_2^+ density for orbits 288 and 292. We can further compare the estimated mean optical depths for the ringlets/plateaus to those derived from stellar occultations by Jerousek et al. (2020), with the values agreeing well (see Table 1).

The fact that these narrow ringlets and plateaus, with widths of 70–250 km and calculated altitudinal shadow extents of just 5–16 km along the trajectory of Cassini (traveling at a velocity of $\sim$34 km s^{-1}), are clearly visible in the H_2^+ data is consistent with the short-lived nature of these ions ($\sim$0.5 s) and low ion flow speeds near periapsis for orbits 288 and 292. The lack of shadow signatures in H_2^+ data for orbits 283 and 287, for which Cassini traversed the shadowed regions at much higher altitudes (and hence lower H_2 densities), can be attributed to the much longer chemical lifetime of H_2^+ at these altitudes, which allows for transport processes to dilute any potential signatures. A rough estimate for a lower limit of the ion flow speed gives $\sim$0.3 km s^{-1} around $\sim$3400 km along Cassini's trajectory, which is in line with a 1 km s^{-1} estimate by Cravens et al. (2019). Similarly, the electron densities for all four analyzed orbits do not show any clear shadowing signatures (dips), as expected from their long chemical (recombination) lifetimes.

The authors thank Lina Hadid, Mark Showalter and the two anonymous referees for their helpful feedback. J.D. is thankful for being supported by the Swedish National Space Agency under grant Dnr 143/18. O.S. acknowledges funding by SNSA Dnr 195/20. F.L.J. acknowledges funding by Lennanders Grant.

Cassini ephemeris data are available from NASA's Planetary Data System (PDS, https://pds-rings.seti.org/tools/ephem2_satc.shtml), last access: 11 August 2021. Cassini RPWS data likewise are available from the PDS. The derived INMS ion data used in the present study were provided by the INMS science team, which is based on the INMS L1A data that is available from the PDS as well.

Appendix A
Derivation of Equation (3)

Define for simplicity $R_{\rm Cass} = R_{\rm Saturn} + {\rm A}_{\rm Cass}$ as the sum of Saturn's radius (at the given subspacecraft latitude and longitude) and Cassini's altitude above the 1 bar level, and consider a coordinate system with origin in Saturn's center, with the z-axis going through the rotational axis and with the xy-plane containing the ring plane (Figure 2). The projection of the x-axis onto the ecliptic points to the Sun (meaning the x-axis would be along the Saturn–Sun line for $\phi_\odot = 0°$). The shortest distance of Cassini to the ring plane is governed solely by its planetocentric latitude θ and given by $z_{\rm Cass} = R_{\rm Cass}\sin\theta$. The projection of the radius vector onto the ring plane is $R_{\rm Cass}\cos\theta$, which can be decomposed into x and y components depending on the hour angle such that $x_{\rm Cass} = R_{\rm Cass}\cos\theta\cos h_\odot$ and $y_{\rm Cass} = R_{\rm Cass}\cos\theta\sin h_\odot$. Due to the Sun's great distance, we take the projection of the sunlight ray onto the ring plane to be parallel to the x-axis, meaning that $y_{\rm cross} = y_{\rm Cass} = R_{\rm Cass}\cos\theta\sin h_\odot$. When viewed in the xz-plane the sunlight crosses the ring plane at angle $\phi_\odot$. A right-angled triangle emerges with a height $z_{\rm Cass}$ against the angle $\phi_\odot$ meaning that the the other leg (parallel to the x-axis) has a length of $x' = z_{\rm Cass}/\tan\phi_\odot = R_{\rm Cass}\sin\theta/\tan\phi_\odot$. Adding this length to $x_{\rm Cass}$ we find $x_{\rm cross} = x_{\rm Cass} + x' = R_{\rm Cass}\cos\theta\cos h_\odot + R_{\rm Cass}\sin\theta/\tan\phi_\odot$. Finally the sought distance from the origin to the point where the line between the Sun and Cassini crosses the ring plane is given by $R_{\rm cross} = \sqrt{x_{\rm cross}^2 + y_{\rm cross}^2}$. With $x_{\rm cross}$ and $y_{\rm cross}$ given as above, Equation (3) readily follows.

Appendix B
Polynomial Fit Parameters

As described in Section 2, Equation (3) was fitted with a quartic polynomial, which enables input of any given ringlet/plateau distance and immediate calculation of the respective shadowed altitudes along Cassini's trajectory. The fit parameters for the following relation are summarized below in Table 2:

$$A_{\rm Cass} = p_1 \times R_{\rm Cross}^4 + p_2 \times R_{\rm Cross}^3 + p_3 \times R_{\rm Cross}^2 + p_4 \times R_{\rm Cross} + p_5. \quad \text{(B1)}$$

For the purpose of estimating the optical depths of the ringlets/plateaus as described in Section 3, the H_2^+ densities from the inbound part of orbit 292 were also fitted with a quartic polynomial (based on Dreyer et al. 2021), the parameters of which can be found in the last row.

Table 2
Fit Parameters (Rounded to Two Decimals) for the Quartic Polynomial Fit (Equation (B1)) of Equation (3) (Using the Polyfit Function of MATLAB R2020a, Including Centering and Scaling with $\mu_1 = $ mean(x) and $\mu_2 = $ std(x)), with $R_{\rm cross}$ in Kilometers As Input Variable and the Respective Shadowed Altitude $A_{\rm Cass}$ in Kilometers As Output

Orbit	p_1	p_2	p_3	p_4	p_5	$\mu_1 = \bar{x}$	$\mu_2 = \sigma_x$
283	0.79	6.42	255.84	989.42	3 855.32	95 224.45	10 915.36
287	0.77	5.21	241.84	956.81	3 927.04	95 795.78	10 772.40
288	8.50	41.45	786.77	2 895.22	4 569.69	109 374.74	18 422.21
292	−0.06	7.82	404.66	1 578.54	3 286.82	100 722.72	13 710.33
H_2^+	−0.00113	0.016 96	−0.07268	0.139 31	0.667 57	1 957.292 77	249.129 30

Note. The last row instead gives the fit parameters (rounded to five decimals) for the fit of the H_2^+ number densities per cubic centimeters with altitude in kilometers as the input variable, derived from Dreyer et al. (2021) and shown in the right panel of Figure 4.

Appendix C
INMS Timestamp Shift

During the investigation of the apparent offset between calculated shadowed altitudes along Cassini's trajectory and the dips in the H_2^+ data, we identified an internal timing error for INMS that accounts for most of this shift. The drift or offset of the spacecraft clock is continuously monitored throughout the mission and, with some delay, made available to the instrument teams. When comparing RPWS, Cassini's Dual Technique Magnetometer and INMS, we discovered that INMS was using a form of correction for the spacecraft clock that was internal to the instrument team and no longer maintained, which accounted for an error up to (−)4 s at the end of the mission, as shown in Figure 6. Although the timing error is minimal for most of the mission, these errors grow toward the end of the mission, which is the data we treat in this study. The timing offsets at periapsis for orbits 283, 287, 288, and 292 are −3.62, −3.78, −3.82, and −3.98 s, respectively. The mean additional timestamp drift between consecutive periapsides in the Grand Finale is −0.04 s.

A separate test of the timestamps was performed by comparing the INMS-measured H^+ densities with the electron densities measured by the Langmuir Probe (LP). These should in theory follow each other quite closely, at least at altitudes where H^+ is the dominant ion species ($\gtrsim$2300 km). The following Figure 7 shows examples for this independent test of the potential timestamp offset discussed in Section 3 by comparing INMS H^+ with LP 20 Hz electron data. The INMS data are shifted by −3.98 s for orbit 292, and subsequent correlation analysis of multiple 20 Hz batches and shift values revealed a correlation peak at −1.05 s additional shift (for a total of −5.03 s for orbit 292). It should be noted that this last second of additional shift is based on both LP 20 Hz data and INMS H^+ data, and could therefore also contain an error component of the LP timestamps. As can be seen in Figure 7, the blue ion data (shifted by an additional −1.05 s) correlates much better with the LP 20 Hz electron density. Considering that the calculated shadowed altitudes along Cassini's trajectory also agree better with some additional shift component of ∼−1 s, it seems likely that there is some additional systematic offset in the INMS timestamps on top of the values shown in Figure 6. We have thus chosen to add this additional offset of −1.05 s for our analysis. The identified timestamp errors affect the archived INMS L1A data on the PDS, and a memo should be provided in due time.

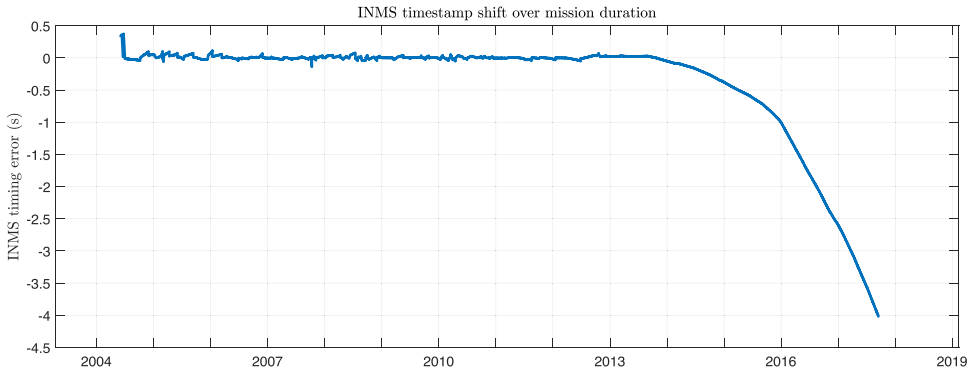

Figure 6. INMS timing compared to simultaneous and offset corrected spacecraft clock over Cassini's mission duration (spacecraft clock−INMS). Since 2013, the INMS timestamps have been increasingly diverging from the spacecraft clock.

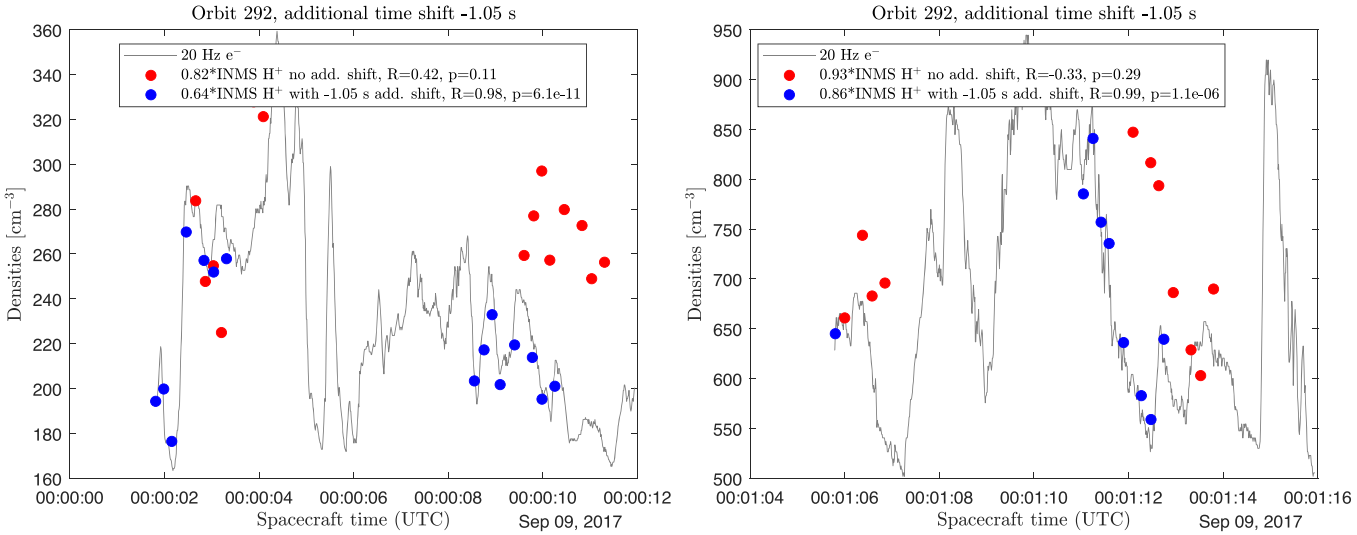

Figure 7. INMS-measured H^+ (blue and red dots) and LP 20 Hz electron (gray line) number densities for orbits 292 inbound for two example periods of 12 s each. The red dots show the original data (after shifting by −3.98 s as shown in Figure 6), the blue dots are shifted by an additional −1.05 s. This value was chosen from a correlation analysis of multiple 20 Hz measurements and shift values. In both cases (red and blue), the first H^+ data point is fixed to the electron density to aid with visual comparison of the correlation. This does not affect the computational correlation analysis.

Appendix D
Data from Orbits 283 and 287

Ion and electron data from the outbound parts of orbits 283 and 287 are shown in Figure 8. No clear ringlet/plateau shadowing signatures are visible in either the INMS H_2^+ data or the LP 20 Hz electron data. This is likely due to the extended lifetimes of both species at the much higher altitudes for closest approach during these two orbits, which allows for transport processes to dilute any narrow shadowing signatures. Note the same reasoning also applies to the lack of electron density signatures for orbits 288 and 292 shown in Figure 4, even at the lower altitudes reached during those orbits.

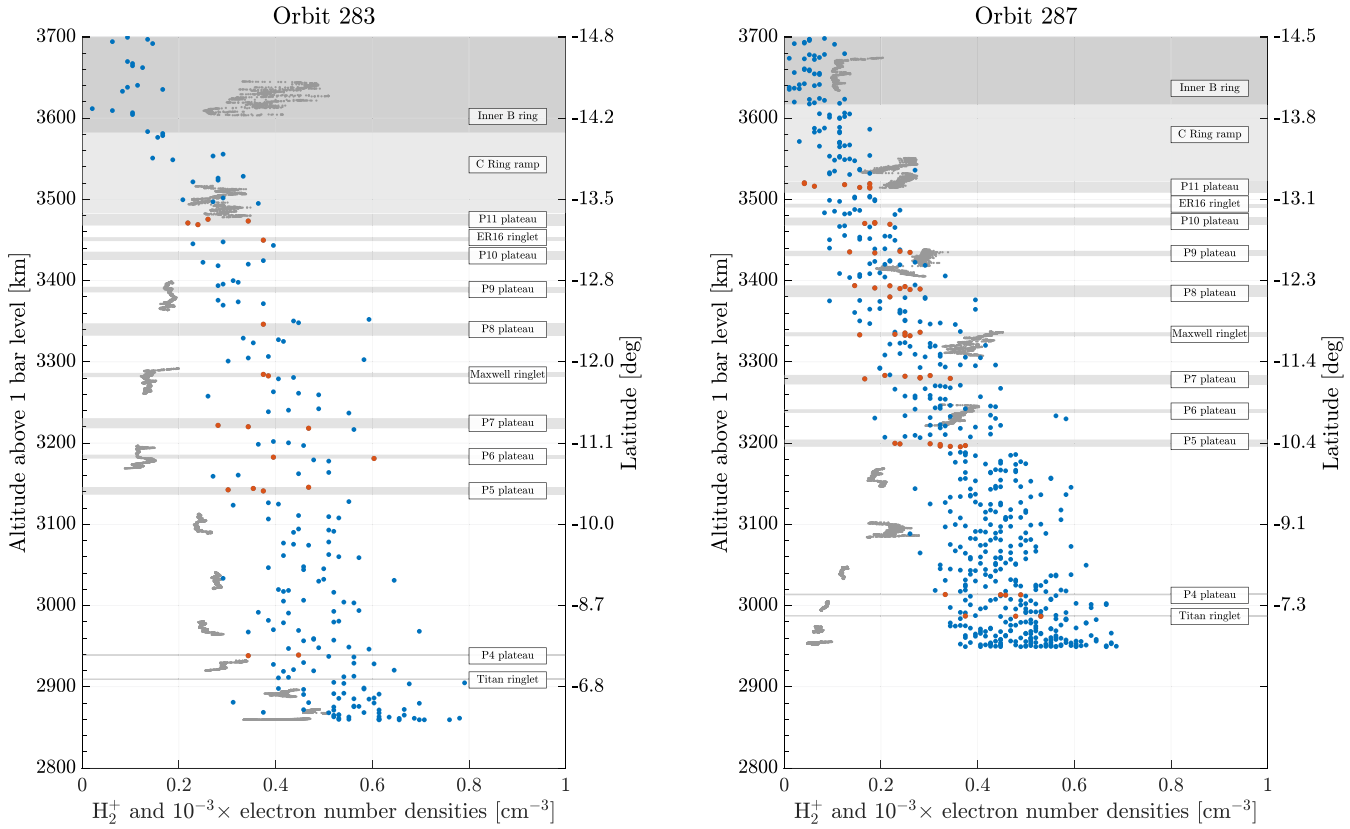

Figure 8. INMS-measured H^+ (blue and red dots with the same coding as in Figure 4) and LP 20 Hz electron (gray dots, scaled with a factor of 10^{-3}) number densities for the outbound parts of orbits 283 and 287 between closest approach and 3700 km, using a time shift for the ion data as described in Appendix C. The corresponding latitudes for each 100 km step are given on the right-hand *y*-axes. Calculated shadows of major ringlets and plateaus in the C ring are shown as shaded areas, with the C ring ramp followed by the inner B ring visible at the upper altitudes. No clear shadowing signatures are visible in either data for both orbits.

ORCID iDs

Joshua Dreyer https://orcid.org/0000-0003-3038-3359
Erik Vigren https://orcid.org/0000-0003-2647-8259
Fredrik L. Johansson https://orcid.org/0000-0002-5386-8255
Oleg Shebanits https://orcid.org/0000-0001-9621-211X
Michiko Morooka https://orcid.org/0000-0001-9958-0241
Jan-Erik Wahlund https://orcid.org/0000-0002-2107-5859
Rebecca S. Perryman https://orcid.org/0000-0003-1858-4692
Jack Hunter Waite https://orcid.org/0000-0002-1978-1025

References

Colwell, J. E., Nicholson, P. D., Tiscareno, M. S., et al. 2009, in Saturn from Cassini-Huygens, ed. M. K. Dougherty, L. W. Esposito, & S. M. Krimigis (Dordrecht: Springer), 375
Cravens, T. E., Morooka, M., Renzaglia, A., et al. 2019, JGRA, 124, 4881
Cuzzi, J. N., Filacchione, G., & Marouf, E. A. 2018, in Planetary Ring Systems. Properties, Structure, and Evolution, ed. M. S. Tiscareno & C. D. Murray (Cambridge: Cambridge Univ. Press), 51
Dreyer, J., Vigren, E., Morooka, M., et al. 2021, PSJ, 2, 39
French, R. G., Nicholson, P. D., Hedman, M. M., et al. 2016, Icar, 279, 62
Gurnett, D. A., Kurth, W. S., Kirchner, D. L., et al. 2004, SSRv, 114, 395
Hadid, L. Z., Morooka, M. W., Wahlund, J., et al. 2018, GeoRL, 45, 10,084
Hadid, L. Z., Morooka, M. W., Wahlund, J., et al. 2019, GeoRL, 46, 9362
Hsu, H. W., Schmidt, J., Kempf, S., et al. 2018, Sci, 362, aat3185
Hunt, G. J., Provan, G., Bunce, E. J., et al. 2018, JGRA, 123, 3806
Jerousek, R. G., Colwell, J. E., & Esposito, L. W. 2011, Icar, 216, 280
Jerousek, R. G., Colwell, J. E., Hedman, M. M., et al. 2020, Icar, 344, 113565
Militzer, B., Wahl, S., & Hubbard, W. B. 2019, ApJ, 879, 78
Mitchell, D. G., Perry, M. E., Hamilton, D. C., et al. 2018, Sci, 362, aat2236
Moore, L., Cravens, T. E., Müller-Wodarg, I., et al. 2018, GeoRL, 45, 9398
Morooka, M. W., Wahlund, J., Hadid, L. Z., et al. 2019, JGRA, 124 1679
Nicholson, P. D., Ansty, T., Hedman, M. M., et al. 2020, Icar, 344, 113356
O'Donoghue, J., Moore, L., Connerney, J. E. P., et al. 2017, GeoRL, 44, 11,762
Persoon, A. M., Kurth, W. S., Gurnett, D. A., et al. 2019, GeoRL, 46, 3061
Theard, L. P., & Huntress, W. T. 1974, JChPh, 60, 2840
Wahlund, J., Morooka, M. W., Hadid, L. Z., et al. 2018, Sci, 359, 66
Waite, J. H., Lewis, W. S., Kasprzak, W. T., et al. 2004, SSRv, 114, 113
Waite, J. H., Perryman, R. S., Perry, M. E., et al. 2018, Sci, 362, aat2382